Electronic Supplementary Information

Lipidation Alters the Phase-separation of Resilin-like Polypeptides

Zhe Zhang, Jingjing Ji, Md. Shahadat Hossain, Briah Bailey, Shikha Nangia, Davoud Mozhdehi

snangia@syr.edu; dmozhdeh@syr.edu

Table of Contents

Materials

The pETDuet-1 vector was purchased from EMD Millipore (Billerica, MA). The chemically competent Eb5alpha and BL21(DE3) cells, restriction enzymes, ligase, and corresponding buffers, as well as DNA extraction and purification kits were purchased from New England Biolabs (Ipswich, MA). Isopropyl β-D-1-thiogalactopyranoside (IPTG) was purchased from A. G. Scientific (San Diego, CA). Myristic acid (Lot# SLCB7175), apomyoglobin, sinapinic acid, alpha-cyano-4-hydroxycinnamic acid, ammonium bicarbonate, and trifluoroacetic acid (TFA) were purchased from Sigma-Aldrich (St. Louis, MO). High-performance liquid chromatography-(HPLC) grade acetonitrile, SnakeSkin™ dialysis tubing with 7 K nominal molecular weight cut off (MWCO), mass spectroscopy grade Pierce™ trypsin protease, tryptone, yeast extract, agar, sodium chloride, ampicillin, phosphate buffer saline (PBS), myristic acid, DMSO, urea, N-hydroxysuccinimide (NHS), 1-ethyl-3-(3-dimethylaminopropyl)carbodiimide hydrochloride (EDC) and ethanol were purchased from Thermo Fisher Scientific (Rockford, IL). Mini-PROTEAN® TGX Stain-Free™ Precast Gels, Precision Plus Protein™ All Blue Pre-stained Protein Standard, and Precision Plus Protein™ Unstained Protein Standards were purchased from Bio-Rad Laboratories, Inc. (Hercules, CA). AZdye 488 Cadaverine was from Vector Laboratories (Newark, CA). The carbon-coated grid (CF300-Cu) was purchased from Electron Microscopy Sciences. Deionized water was obtained from a Milli-Q® system (Millipore SAS, France). Simply Blue™ SafeStain was purchased from Novex (Van Allen Way Carlsbad, CA). All chemicals were used as received without further purification. DNA oligos were ordered from Integrated DNA Technologies (Coralville, Iowa).

Cloning and Protein Sequences

pETDuet-1 was used as a bicistronic vector to encode all the necessary elements for N-myristoylation: 1) NMT from S*. cerevisiae* was encoded in multiple cloning site 1, while 2) RLP fused to the peptide substrate of NMT was encoded in multiple cloning site 2. Unmodified RLPs were expressed from control plasmids lacking the NMT gene.

NMT

*(M)*GSSHHHHHHKDHKFWRTQPVKDFDEKVVEEGPIDKPKTPEDISDKPLPLLSSFEWCSIDVD
NKKQLEDVFVLLNENYVEDRDAGFRFNYTKEFFNWALKSPGWKKDWHIGVRVKETQKLVAFIS
AIPVTLGVRGKQVPSVEINFLCVHKQLRSKRLTPVLIKEITRRVNKCDIWHALYTAGIVLPAPVSTC
RYTHRPLNWKKLYEVDFTGLPDGHTEEDMIAENALPAKTKTAGLRKLKKEDIDQVFELFKRYQS
RFELIQIFTKEEFEHNFIGEESLPLDKQVIFSYVVEQPDGKITDFFSFYSLPFTILNNTKYKDLGIGY
LYYYATDADFQFKDRFDPKATKALKTRLCELIYDACILAKNANMDVFNALTSQDNTLFLDDLKFG
PGDGFLNFYLFNYRAKPITGGLNPDNSNDIKRRSNVGVVML

***AGA*-RLP:**

*(M)*GAGASRGGSGGSGRGDQPYQGRGDQPYQGRGDQPYQGRGDQPYQGRGDQPYQGRG
DQPYQGRGDQPYQGRGDQPYQGRGDQPYQGRGDQPYQGRGDQPYQGRGDQPYQGRGD
QPYQGRGDQPYQGRGDQPYQGRGDQPYQGRGDQPYQGRGDQPYQGRGDQPYQGRGDQ
PYQGY

***LSL*-RLP:**

*(M)*GLSLSRGGSGGSGRGDQPYQGRGDQPYQGRGDQPYQGRGDQPYQGRGDQPYQGRGD
QPYQGRGDQPYQGRGDQPYQGRGDQPYQGRGDQPYQGRGDQPYQGRGDQPYQGRGDQ
PYQGRGDQPYQGRGDQPYQGRGDQPYQGRGDQPYQGRGDQPYQGRGDQPYQGRGDQPYQ
GRGDQPYQGY

Protein Expression and Purification

All proteins were expressed in the *E. coli* BL21(DE3) *strain* by following a previously established protocol.[1] Cells were grown in 2x YT media with 100 µg/mL of ampicillin until OD_{600} ~ 0.8-1. The temperature was then reduced to 28°C, and the expression culture was supplemented with myristic acid (200 µM) and IPTG (500 µM). After 8 h, cells were harvested by centrifugation (4000 × g, 30 min, 4 °C), resuspended in phosphate buffer saline (PBS, 10 mL per 1 L of culture), and lysed by sonication. The lysed bacterial suspension was chilled on ice for 15 min to induce the phase separation of RLPs and subsequently centrifuged (22,830 × g, 4 °C, 15 min) to RLP condensates from soluble endogenous proteins. After discarding the supernatant, the pellet was extracted twice with 20% acetonitrile solution to separate the protein from insoluble membrane fractions. These extracted elutions were pooled and further purified by reversed-phase HPLC (RP-HPLC). The organic solvent was removed by overnight dialysis against water (MWCO = 3.5 kDa). After dialysis, the protein samples were frozen in liquid nitrogen and lyophilized. The absence of acetonitrile in the samples was confirmed by ^{1}H NMR, verifying the efficacy of solvent removal. Moreover, the ^{19}F NMR analysis indicated that only a few TFA adducts (8-10) were present in each sample following purification (data not shown), indicating a mass purity of over 95%, in line with the RP-HPLC data (Figure S4). The concentration of the stock solution of the proteins (in water) was determined using UV-Vis by measuring the

absorbance at 280 nm at temperatures above the UCST (ε= 31290 $M^{-1}cm^{-1}$, calculated by ProtParam suite in Expasy), closely agreeing with gravimetric measurements. Each protein batch underwent characterization through SDS-PAGE, RP-HPLC, MALDI-TOF, and NMR, following the best practices recommended for protein reagents.[2]

Fluorescent Protein Labeling

Proteins were labeled by in situ activation of carboxylic acids using EDC/NHS followed by reaction with AZDye 488 cadaverine dye according to the manufacturer protocol. Briefly, protein (5 mg), EDC (0.1 mg), and NHS (0.12 mg) were dissolved into DMF (1 mL) and stirred at room temperature for 15 minutes. After activation, AZDye 488 (0.16 mg in 500 µL DMF) was added and allowed to react for 1h. The reaction was quenched by the addition of 13.5 mL water and dialyzed against water overnight (MWCO = 3.5 kD). The unreacted fluorophores were removed by chilling the dialysis retentate on ice, followed by centrifugation at 4 °C. This promoted the condensation of the labeled proteins, which were isolated as a pellet, while the unreacted dye stayed in the supernatant. The protein pellets were resuspended in water and lyophilized for storage.

Matrix-Assisted Laser Desorption/Ionization Time-of-Flight Mass Spectrometry (MALDI-TOF-MS)

MALDI-TOF-MS was conducted on Bruker microflex LRF with a microScout ion source using sinapinic acid or α-cyano-4-hydroxycinnamic acid (CHCA) as matrix. All spectra were calibrated using apomyoglobin (M_W= 16 952 Da) or bradykinin fragment 1-7 (M_W= 757.3997 Da). N-terminal peptide fragments were characterized by MALDI-TOF-MS after digestion with trypsin for 3h in 50 mM ammonium bicarbonate buffer (pH= 7.8).

Reversed-phase High-performance Liquid Chromatography (RP-HPLC)

Analytical and preparative RP-HPLC was performed on a Shimadzu instrument equipped with a detector at wavelengths of 190 and 280 nm using a linear gradient of acetonitrile in water (0-90% over 40 min) and supplemented with 0.1% TFA as the mobile phase. The proteins were purified and analyzed using C18 HPLC columns (Phenomenex Jupiter® 5 µm C18 300 Å, 250 × 10 mm and Phenomenex Jupiter® 5 µm C18 300 Å, 250 × 4.6 mm).

Turbidimetry Assay

The temperature-triggered phase separation of proteins was monitored using a UV-Vis Spectrophotometer (Cary100, Agilent) equipped with a Peltier temperature controller. Proteins were prepared at different concentrations and equilibrated at 80°C (T > UCST). The solution turbidity was measured as a function of temperature by measuring the absorbance at 350 nm while cooling the solution at the rate of 1 °C/min.

Van't Hoff Analysis

Van't Hoff analysis estimates enthalpy (ΔH) and entropy (ΔS) of reversible processes by analyzing temperature-dependent changes in equilibrium constant (K_{eq}). It relates these changes to thermodynamic parameters using: $\Delta G = -RT \ln(K_{eq}) = \Delta H - T\Delta S$, where ΔG is Gibbs free energy change, R is the universal gas constant (8.314 J/(mol·K)), and T is temperature in Kelvin. Rearranging yields the linear Van't Hoff equation: $\ln(K_{eq}) = -\Delta H/(RT) + \Delta S/R$, allowing ΔH and ΔS estimation from equilibrium constant measurements across temperatures.

In this context, phase separation can be conceptualized as a reaction in which the solubility of the protein is altered at cloud point (T_c), leading to condensate formation.[3, 4] Assuming the protein concentration in the condensed phase is significantly higher and constant, K_{eq} is defined by the protein concentration in the dilute phase, indicated as C* (M). This simplification leads to

the equation: $\ln(C^*) = -(\Delta H/R)(1/T_c) + (\Delta S/R)$. Applying a linear regression to $\ln(C^*)$ vs. $1/T_c$ data enables the estimation of ΔH and ΔS from the slope and intercept, respectively.

Dynamic Light Scattering (DLS)

DLS was conducted on a NanoLab 3D (LS Instruments, Switzerland) with a 90° detector. The following sample preparation procedure was used to obtain reproducible DLS data. First, the protein stock solutions were prepared by dissolving the lyophilized proteins in water. The stock solution was heated to 80 °C for 10 min and quickly filtered through 0.2 μm PVDF filters. The dissolution in water at elevated temperatures results in smaller aggregates due to repulsion between charged RLP chains, preventing significant loss of analytes during filtration. The concentration of the filtered solution was quantified by A280 and then buffered by the addition of concentrated PBS buffer (10X PBS, prefiltered) at 80 °C, which resulted in a final protein concentration of 10μM in 1X PBS. Samples were transferred to DLS cuvettes and the experiment was conducted by cooling the sample from T_{high} = UCST + 20 °C to T_{low} = UCST-10°C at 1°C increment. The samples were equilibrated at each temperature for 1 minute. Measurements were conducted in triplicate at each temperature. Scattering correlation functions were analyzed with NanoLab 3D software using cumulant fit to calculate the hydrodynamic radius (Rh).

Cryo-Transmission Electron Microscopy (Cryo-TEM)

Protein solutions (100 μM in PBS) were incubated above T_c for 10 min and then cooled to 25 °C. Then, samples were deposited to plasma-treated TEM grids. After plunge-freezing in liquid ethane, grids were imaged on a Tecnai BioTwin 120kV transmission electron microscope. Images were collected on a Gatan SC1000A charge-coupled device camera and analyzed using ImageJ. It is important to note Cryo-TEM, which preserves samples in vitreous ice, excels at capturing nano-scale details but the entire condensate is likely not included within the thin

vitrified ice layer. This limitation results in an underestimation of condensates size in cryo-TEM images.

Attenuated Total Reflection-Fourier Transform Infrared Spectroscopy (ATR FT-IR)

The ATR FT-IR spectra were collected using Thermo Scientific Nicolet iS5 FT-IR Spectrometer with iD7 attenuated total reflectance accessory. The resolution was set to 4 cm^{-1} and 64 scans were conducted for each spectrum. The samples were prepared in deuterated PBS at 200 μM. The spectra of lipidated and unmodified RLP condensates were collected at 25 °C which is below the transition temperature of all constructs at this concentration. The background spectrum for deuterated PBS was collected and subtracted from each condensate spectrum. A baseline correction (straight line between the endpoints) and normalization based on the curve areas was also conducted using OriginPro 2021b (OriginLab Corporation, Northampton, MA, USA).

Fluorescence Recovery After Photobleaching (FRAP)

Fluorescent-labeled protein samples were prepared by mixing labeled protein with unlabeled protein in PBS to the final concentration of 100μM (5% labeled protein). The FRAP was conducted on Zeiss LSM 980 with Airyscan 2 confocal microscope. The samples were bleached with 405 nm, 488 nm, and 561 nm laser (80% intensity) at the fourth frame, and the intensity of the bleached area was monitored for 1 minute (unmodified RLPs) or 6 minutes (lipidated RLPs). The intensity data was processed through ImageJ by normalizing the bleached area intensity with the unbleached area following Eq. S1 to eliminate the effect of unwanted bleaching during the imaging.

$$Norm(t) = \frac{Ref_{pre-bleach}}{Ref(t)} \cdot \frac{FRAP(t)}{FRAP_{pre-bleach}} \qquad \text{(Eq. S1)}$$

Where FRAP(t) and Ref(t) corresponds to the intensity of FRAP region and unbleached region in each frame, $FRAP_{pre\text{-}bleach}$ and $Ref_{pre\text{-}bleach}$ corresponds to the intensity of each region before bleach.

The fluorescence recovery was quantified by fitting the normalized FRAP to an exponential model:

$$y(t) = A \cdot (1 - e^{-\tau \cdot t}) \qquad \text{(Eq. S2)}$$

Where A is the plateau intensity, τ is a fitted parameter and t is time after bleach.

The half time of recovery ($t_{1/2}$) was obtained using the following equation:

$$t_{1/2} = \frac{ln0.5}{-\tau} \qquad \text{(Eq. S3)}$$

Where τ corresponds to the fitted parameter in Eq. S2.[5]

Computational Details

The atomistic structures of disordered peptides fused to the lipidation sites were obtained from I-TASSER (Iterative Threading ASSEmbly Refinement) server.[6-8] The myristoyl group is added in CHARMM-GUI solution builder. The systems were subjected to a series of energy minimization and equilibration steps with the input files generated from CHARMM-GUI solution builder,[9-11] where disordered peptides allowed to be modified by myristic acids to generate lipidated peptide systems. The CHARMM36m force field[12] parameters were used for lipidated proteins, salt (0.15 M NaCl), and explicit TIP3P water. The atomistic molecular dynamics (MD) simulations were performed using the GROMACS version 2019.[13] Each system was energy minimized, followed by equilibration in isothermal-isochoric (*NVT*) and isothermal-isobaric (*NPT*) for 1 ns each, and production MD run under *NPT* conditions for 3 μs. The heavy atoms of the lipidated proteins were restrained during *NVT* and *NPT* equilibration. All restraints were removed during the production MD. The temperature was maintained at 40 °C using the v-rescale thermostat[14] with τ_t = 1.0 ps.

In the pre-production *NPT* run, isotropic pressure of 1 bar was maintained using Berendsen barostat[15] with τ_p = 5.0 ps and compressibility of 4.5×10^{-5} bar^{-1}. In the production MD, we used the Parrinello-Rahman barostat[16] with τ_p = 5.0 ps and compressibility of 4.5×10^{-5} bar^{-1}. Three-dimensional periodic boundary conditions (PBC) were applied to each system. A 2 fs time step was used, and the nonbonded interaction neighbor list was updated every 20 steps. A 1.2 nm cutoff was used for the electrostatic and van der Waals interactions. The long-range electrostatic interactions were calculated using the Particle-Mesh Ewald (PME) method after a 1.2 nm cutoff. The bonds involving hydrogen atoms were constrained using the linear constraint solver (LINCS) algorithm. Unmodified proteins were simulated for 200 ns at 40 °C with similar simulation parameters.

The equilibrated protein structures were extracted and placed into an empty cubic simulation box. The protein was then rehydrated with a shell of water (average density 0.977 g cm^{-3}) of thickness d_{shell} = 0.415 nm larger than the first hydration shell of water from the protein's surface. Each system was energy-minimized, followed by water evaporation using the PARCH scale annealing protocol,[17] where water is annealed from 27 to 527 °C at constant volume with an annealing rate of 1 °C/10 ps. With the increase in temperature, water molecules evaporate from the protein surface and move within the fixed volume of the box without any positional constraints. The cutoff for calculating the number of water molecules (d_{water}) contacting a residue at any given time is 0.315 nm. However, the protein was position-restrained with a force constant of 1000 kJ mol^{-1} nm^{-2} to maintain the protein's conformation and topography. Similarly, the counter ions were restrained with a force constant of 1000 kJ mol^{-1} nm^{-2} to maintain a constant charge balance around the protein. The parch calculation was performed in triplicates.

Molecular visualization and images were rendered using PyMol[18] and VMD[19] software suites. Data analysis and plotting were performed using in-house Python scripts based on publicly hosted Python packages, such as matplotlib, SciPy, and MDAnalysis.[20]

Supplementary Tables

Table S1. Theoretical molecular weight and observed m/z of each construct.

Construct	Theoretical m/z $[M+H]^+$	Observed m/z $[M+H]^+$
AGA-RLP	19179.8	19177.04
m-*AGA*-RLP	19390.2	19391.3
LSL-RLP	19294.0	19294.9
m-*LSL*-RLP	19504.4	19502.3
Trypsin-digested Fragments		
GAGASR	518.269	518.225
m-GAGASR	728.467	728.544
GLSLSR	632.373	632.386
m-GLSLSR	842.572	842.620

Supplementary Figures

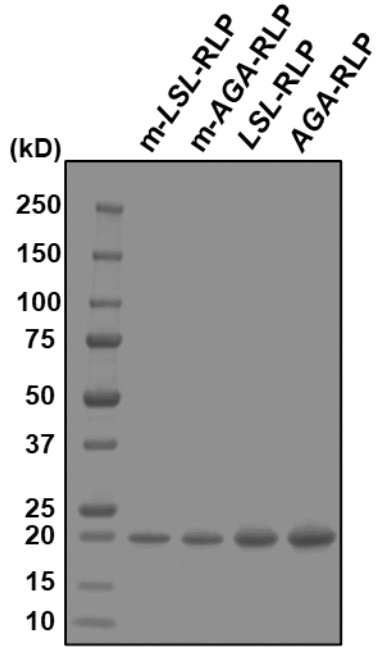

Figure S1. Characterization of purified proteins using SDS-PAGE. Protein bands were stained with SimplyBlue® for visualization.

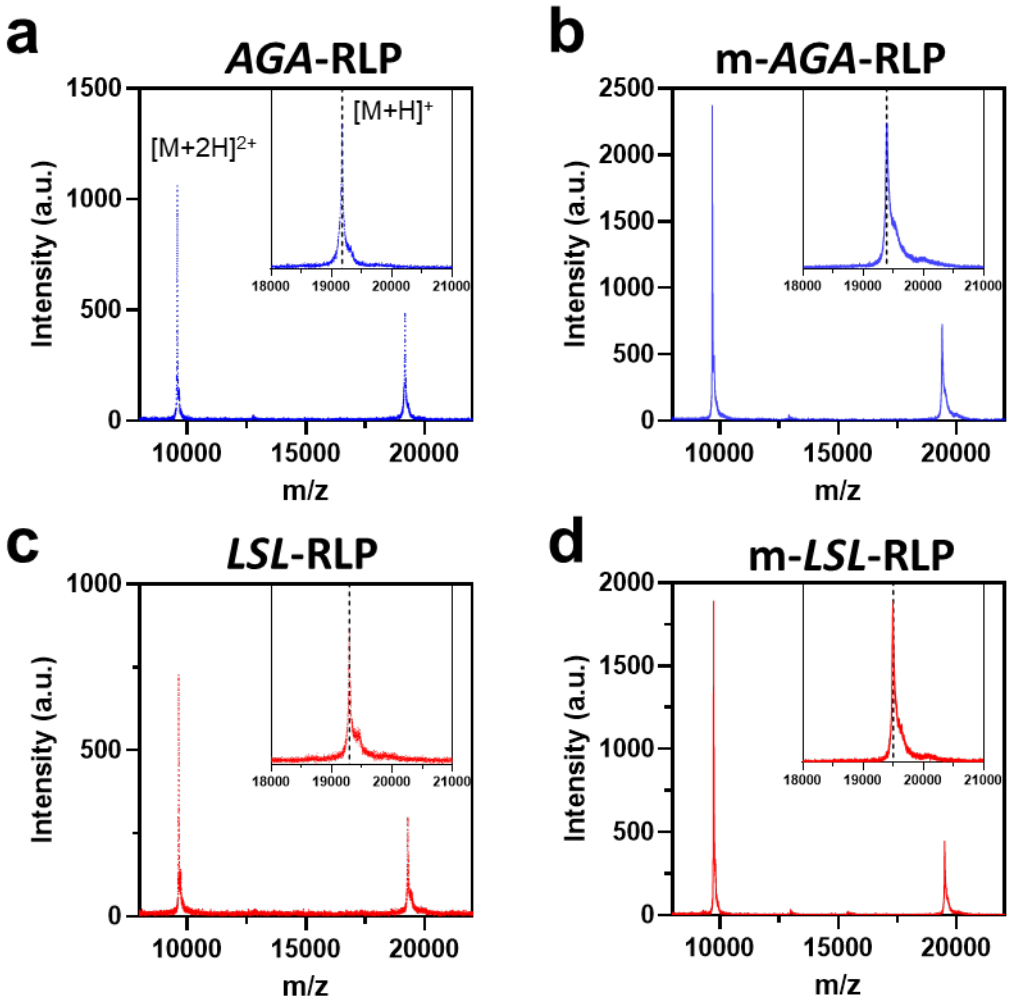

Figure S2. MALDI-TOF-MS spectra of the proteins used in this study. The identity of proteins were confirmed by MALDI-TOF-MS. Both $[M + H]^+$ and $[M + 2H]^{2+}$ peaks were observed in each construct. *AGA*-RLP (a); m-*AGA*-RLP (b); *LSL*-RLP (c) and m-*LSL*-RLP (d). The vertical dashed line represent the theoretical mass of the precursor ion. The theoretical and observed masses are reported in Table S1.

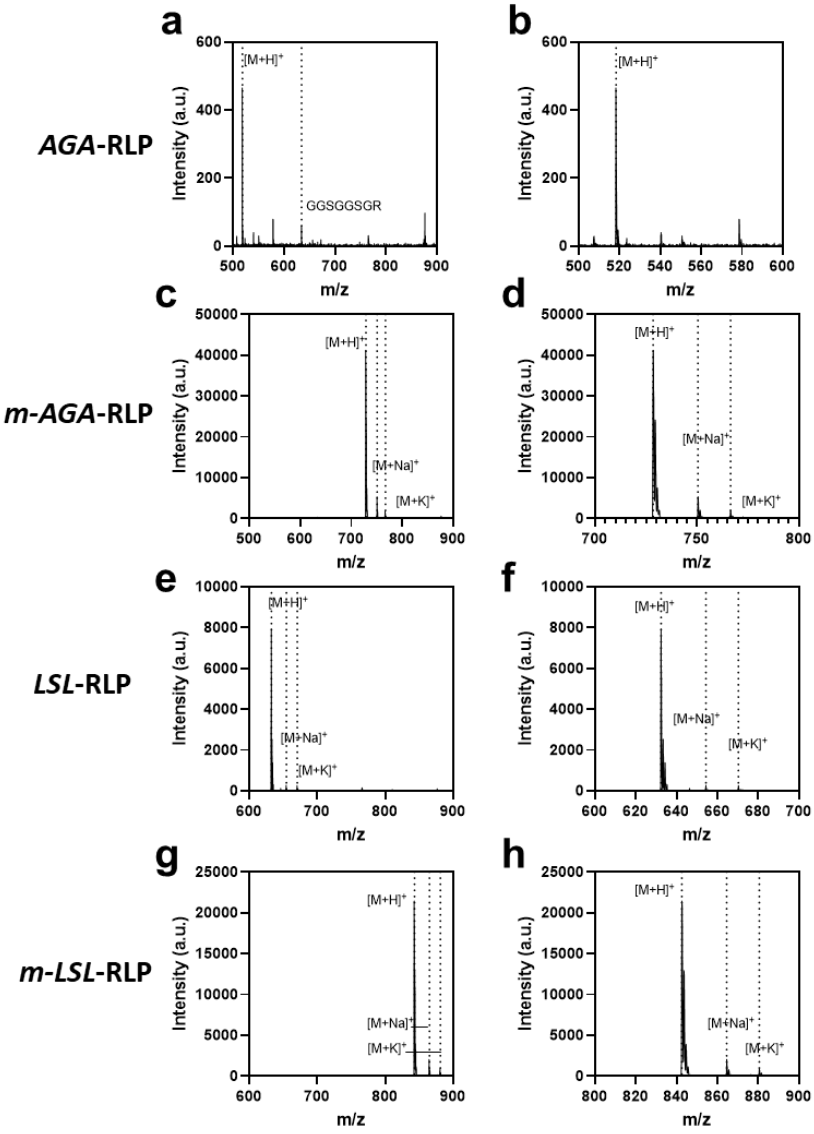

Figure S3. Analysis of N-terminal fragment using MALDI-TOF-MS to confirm myristoylation. The peptide fragments resulting from trypsin digestion were subjected to analysis using MALDI-TOF-MS, *AGA*-RLP (a, b) and m-*AGA*-RLP (c, d); *LSL*-RLP (e, f) and m-*LSL*-RLP (g, h). The mass of the N-terminal fragment increased by 210.276 ± 0.042 Da, which matches the mass of a myristoyl motif. The panels on the right are zoomed-in views around the prominent signal to better highlight the adduct ions. Small, non-labeled peaks arise from matrix adducts. The theoretical and observed masses are presented in Table S1.

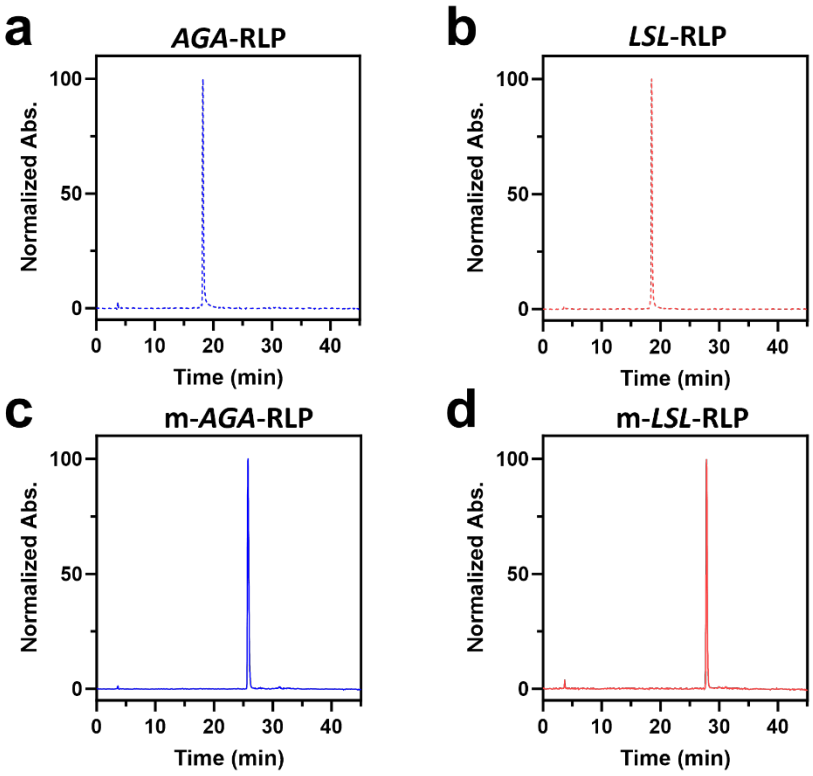

Figure S4. RP-HPLC-based analysis of sample purity and hydrophobicity. The purity of protein samples was confirmed by the presence of a single peak in each chromatogram, indicating the successful separation of unmodified and lipidated isoforms during purification. Myristoylation extended the retention time, consistent with the increased hydrophobicity of lipidated constructs: a) *AGA*-RLP at 18.2 minutes, b) *LSL*-RLP at 18.5 minutes, c) m-*AGA*-RLP at 25.7 minutes, and d) m-*LSL*-RLP at 27.7 minutes. Non-lipidated constructs had similar retention times, while the lipidated isoforms showed a difference of over 2 minutes, indicating a significant increase in hydrophobicity for *LSL*-RLP after lipidation. The small peak at 3.6 min is a system (solvent) peak.

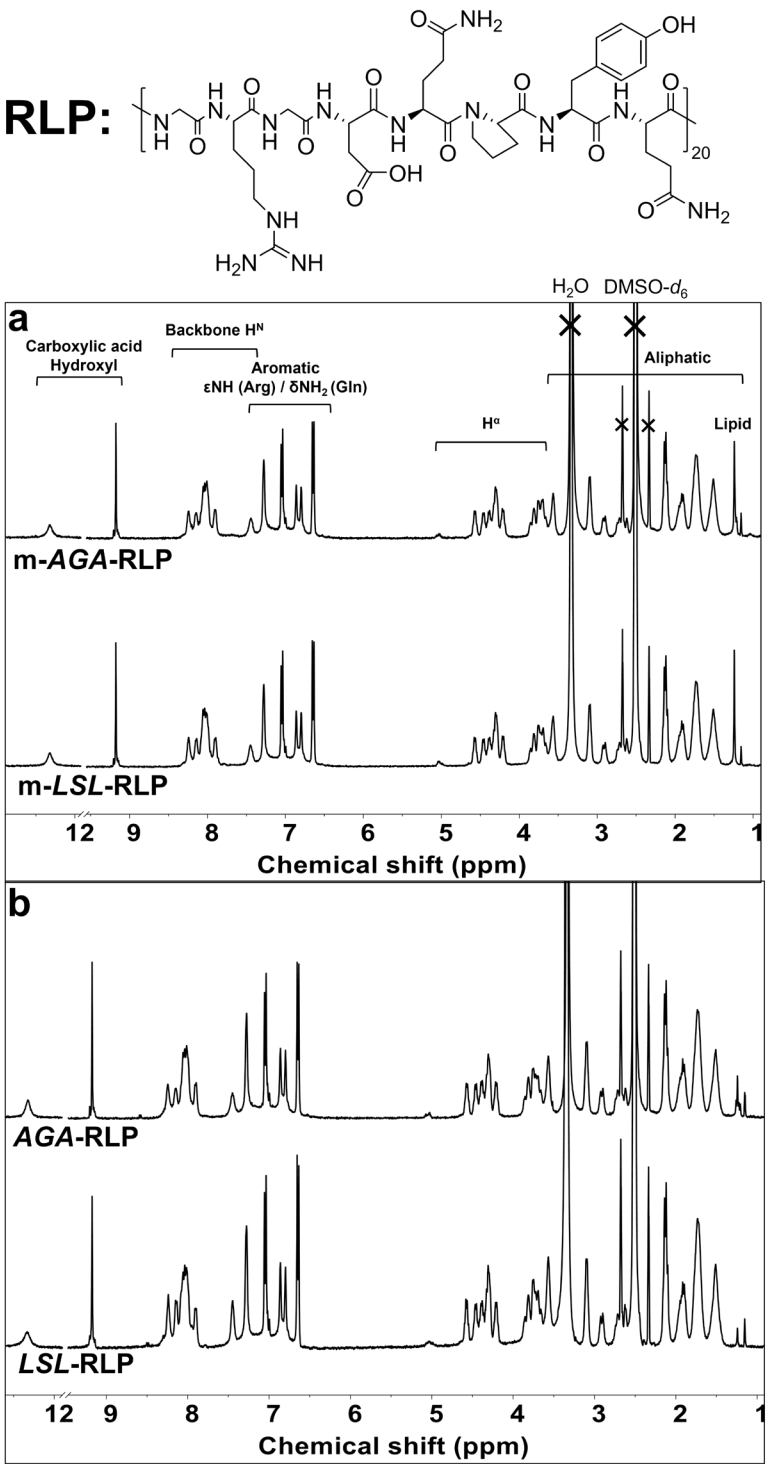

Figure S5. ^{1}H NMR spectra of unmodified and lipidated proteins in DMSO-d$_6$. a) lipidated proteins; b) unmodified proteins. Peaks denoted by 'X' represent signal from water, solvent, and ^{13}C satellite peaks, the latter flanking the main DMSO peak symmetrically.

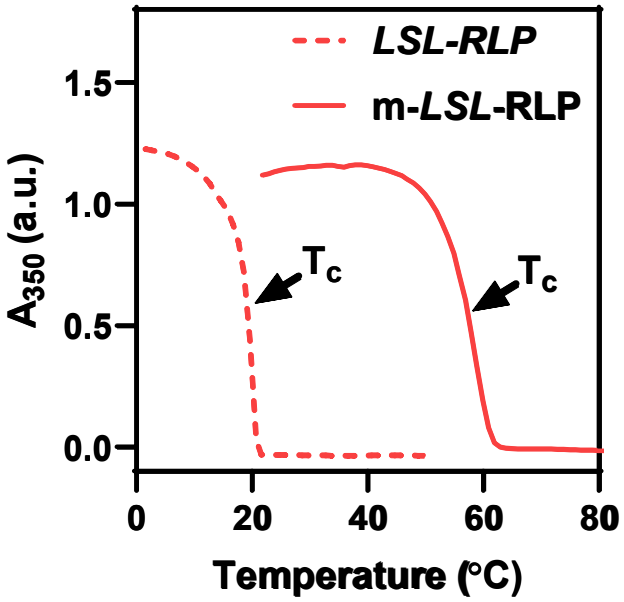

Figure S6. Characterization of the UCST phase behaviour of *LSL*-RLP and m-*LSL*-RLP using variable-temperature turbidimetry. Representative plots for *LSL*-RLP (dashed line) and m-*AGA*-RLP (solid line) at 20 μM in PBS. Arrows indicate their respective cloud temperatures (Tc).

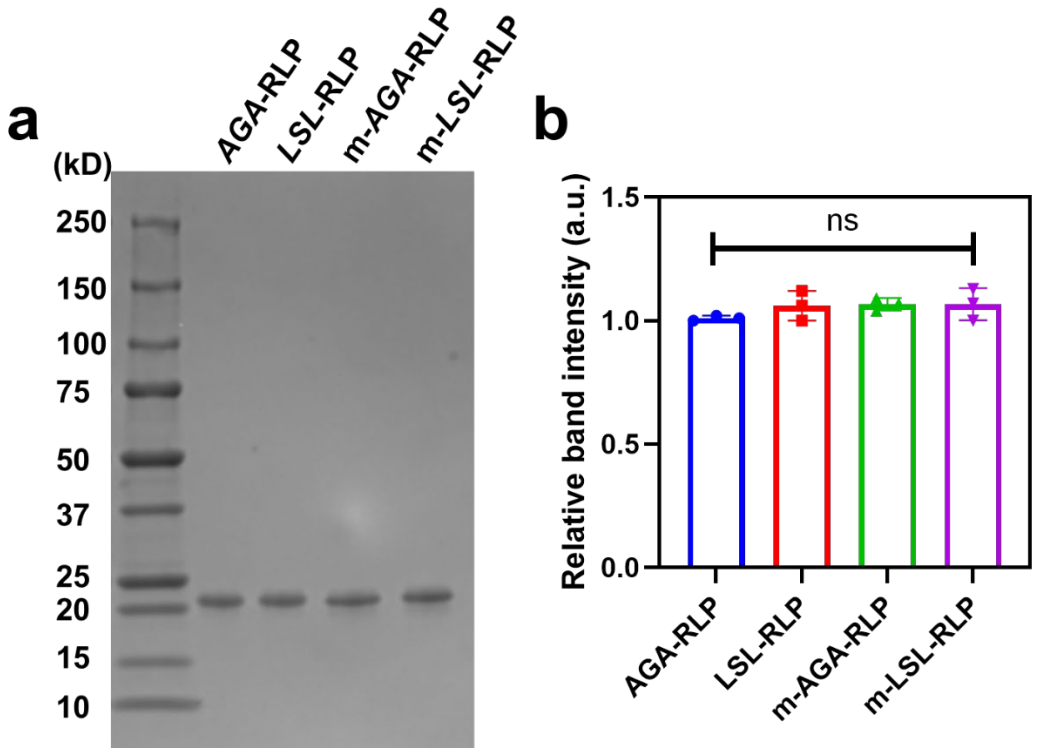

Figure S7. Assessment of protein concentration uniformity through densitometry. Concentrations of stock solutions for each construct were measured with the A280 method (Ext. coefficient is 31290 M^{-1} cm^{-1} for all constructs). These samples were then diluted to 10 μM in PBS, and equal volumes were analyzed via SDS-PAGE. a) A representative gel stained with Coomassie Blue, illustrating the protein bands. b) The relative intensities of these bands were quantified using Bio-Rad Image Lab Software. Bar plots represent the aggregated results from three independent experiments. The absence of statistically significant differences in band intensity ($F(3, 8) = 1.052$, $p = 0.42$) confirms uniform protein concentrations.

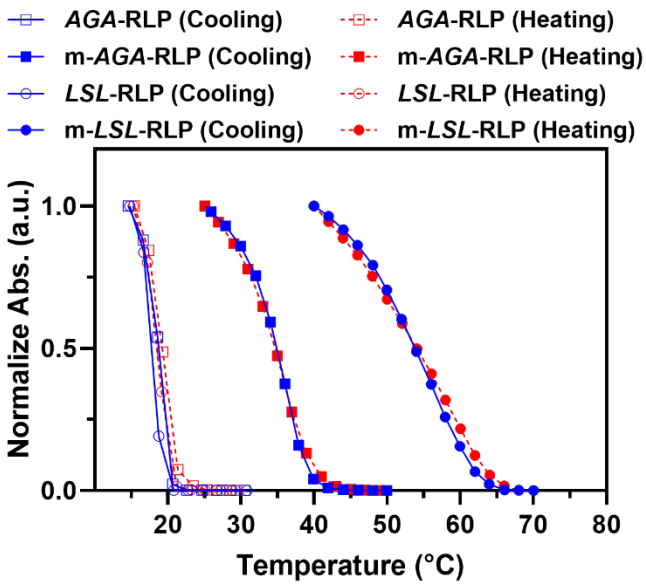

Figure S8. Characterization of the reversibility of the phase-separation for unmodified and lipidated resilins using variable temperature turbidimetry. The overlap of cooling (blue) and heating (red) curves signifies reversible macroscopic phase separation.

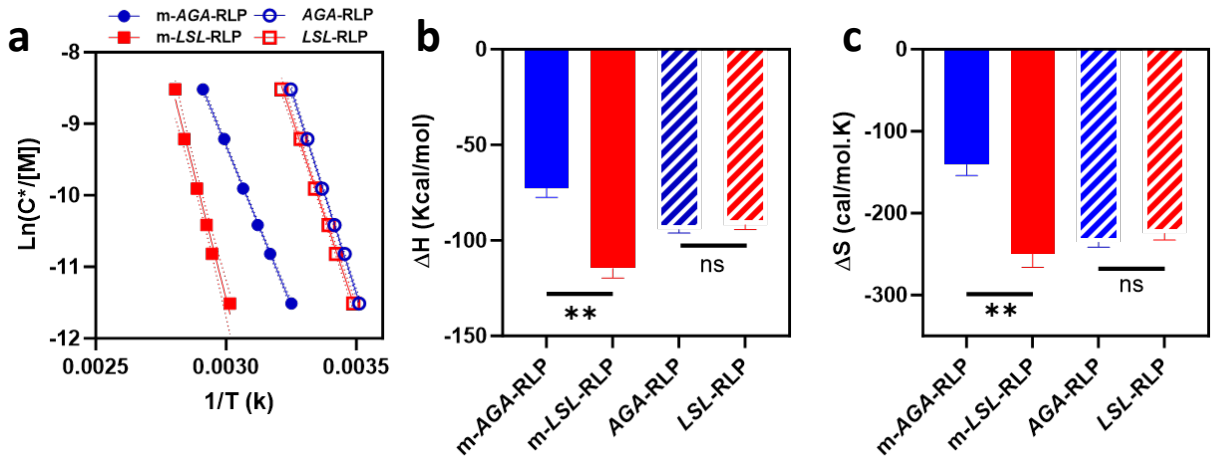

Figure S9. Van't Hoff analysis on cloud points and extracted enthalpic and entropic parameters. (a) Van 't Hoff plot of concentration (natural logarithm) and cloudy point temperature (Inverse). Dotted lines denote 95% confidence intervals in linear regression analysis. Enthalpy change **(b)** is calculated by (slope*R), and entropy change **(c)** is calculated by (- intercept*R) in Van 't Hoff plot. Two-way ANOVA was used to analyze the effects of lipidation and lipidation site sequence on ΔH and ΔS separately. The analysis revealed a statistically significant interaction between lipidation and lipidation site sequence on both ΔH ($F(1, 4) = 69.39$, $p = 0.001$) and ΔS ($F(1, 4) = 51.65$, $p = 0.002$). The Tukey test indicated significant differences between the thermodynamic parameters of m-*AGA*-RLP and m-*LSL*-RLP, ΔH ($p = 0.001$) and ΔS ($p = 0.003$). However, in the absence of the lipid, there were no statistical differences between the constructs, i.e., *AGA*-RLP vs. *LSL*-RLP, ΔH (p = 0.912) or ΔS (p = 0.799).

Supplementary note. Given that the Gibbs free energy of phase separation is zero at the cloud point, $T_c = \Delta H / \Delta S$. Therefore, T_c is determined by the ratio between these two parameters. Our data shows that lipidation impacts both ΔH and ΔS, mediated by enhanced hydrophobic interactions and alterations in protein self-assembly across both dilute and condensed phases. It is important to note that while lipid-mediated organization is expected to decrease the entropy of the polypeptide chain in solution above the UCST (as micelles exhibit lower entropy compared to free chains), the ΔS in this analysis specifically pertains to entropy changes during phase separation. This highlights the necessity of examining the thermodynamics of the protein chain in both phases to fully account for the observed changes.

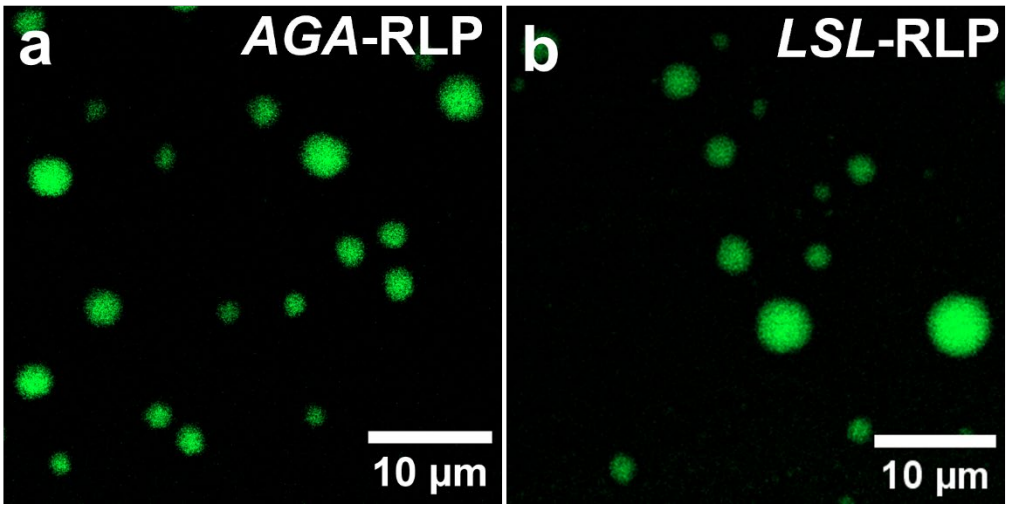

Figure S10. Morphology of unmodified RLP under fluorescent confocal microscopy. non-lipidated *AGA*-RLP (a) and *LSL*-RLP (b) condensate exhited cannonical droplets at room temperature. [Protein] = 100 µM in PBS.

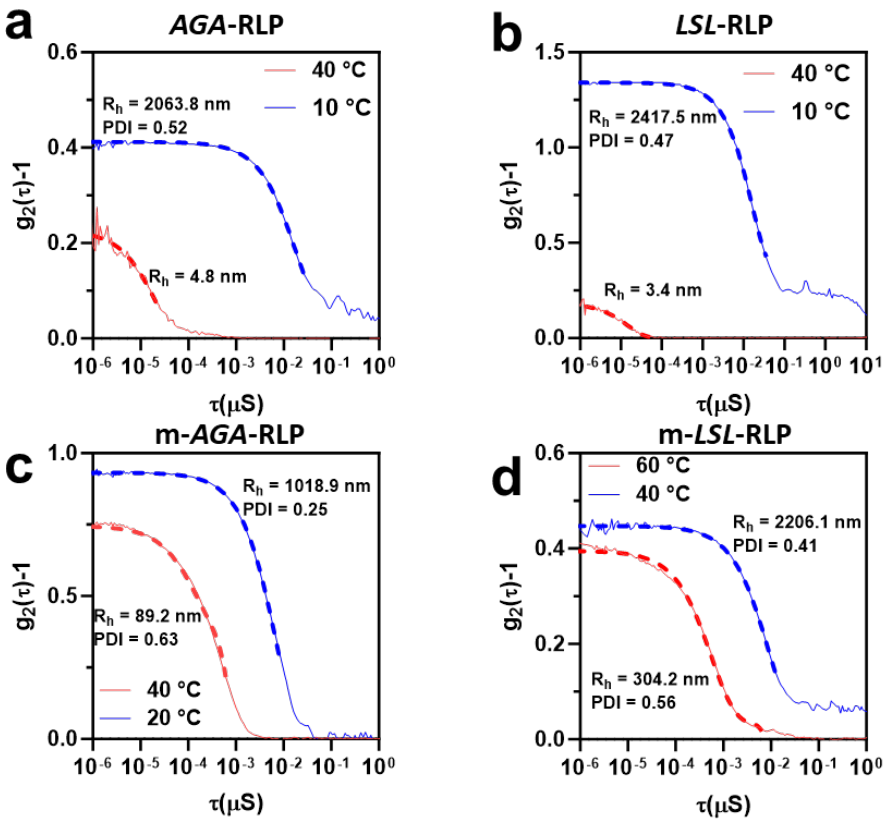

Figure S11. DLS autocorrelation functions for each construct at temperatures above and below the UCST, with cumulant fit depicted by dashed lines. Hydrodynamic radius (R_h) and polydispersity index (PDI) are detailed for each profile. a) *AGA*-RLP; b) *LSL*-RLP; c) m-*AGA*-RLP; and d) m-*LSL*-RLP. For non-lipidated samples at higher temperatures, fitting was performed using a first-order equation, which does not report a PDI.

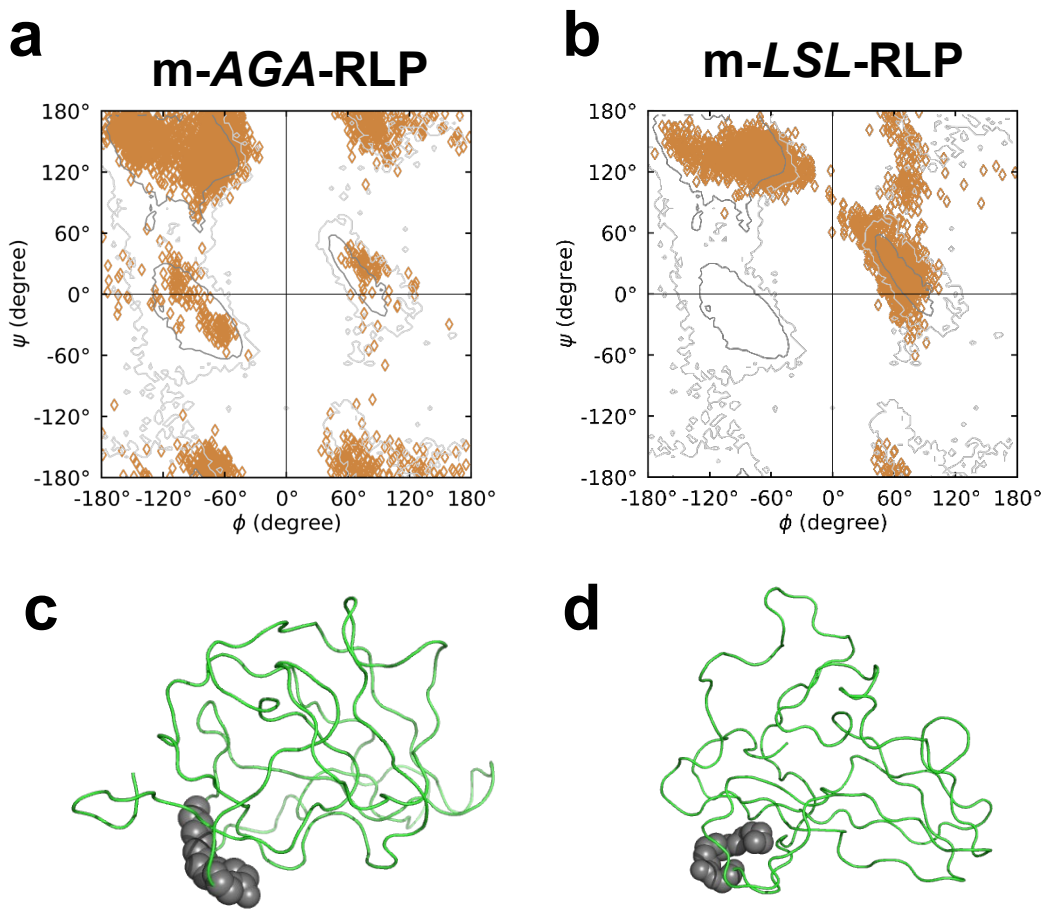

Figure S12. Analysis of the secondary structure of myristoylated constructs in molecular dynamics simulations. The Ramachandran plots for m-*AGA*-RLP (a) and m-*LSL*-RLP (b) at 40°C. Representative 3D structures of m-*AGA*-RLP (c) and m-*LSL*-RLP (d) show predominantely random coil conformations.

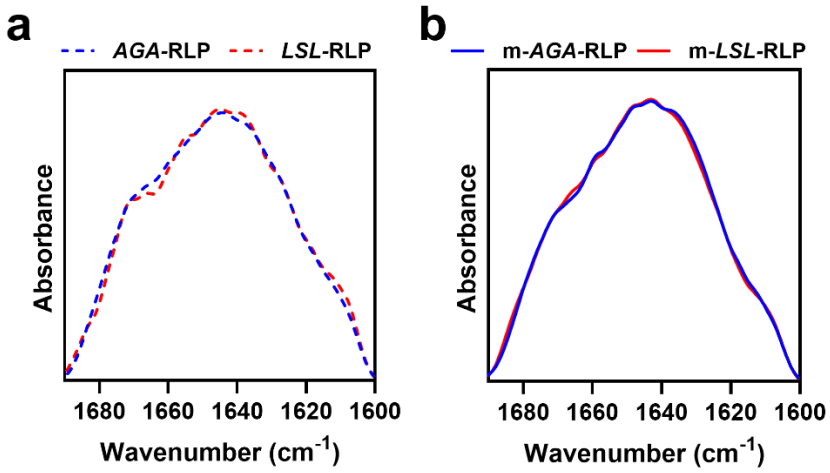

Figure S13. Assessment of the secondary structures of lipidated and unmodified RLP condensates using ATR-FTIR spectroscopy. The FT-IR spectra at 25°C were nearly identical between a) unlipidated and b) lipidated constructs, showing that the changes in the sequence of the lipidation site does not alter the overall secondary structure of RLPs. [Protein] = 200 μM in deutrated PBS.

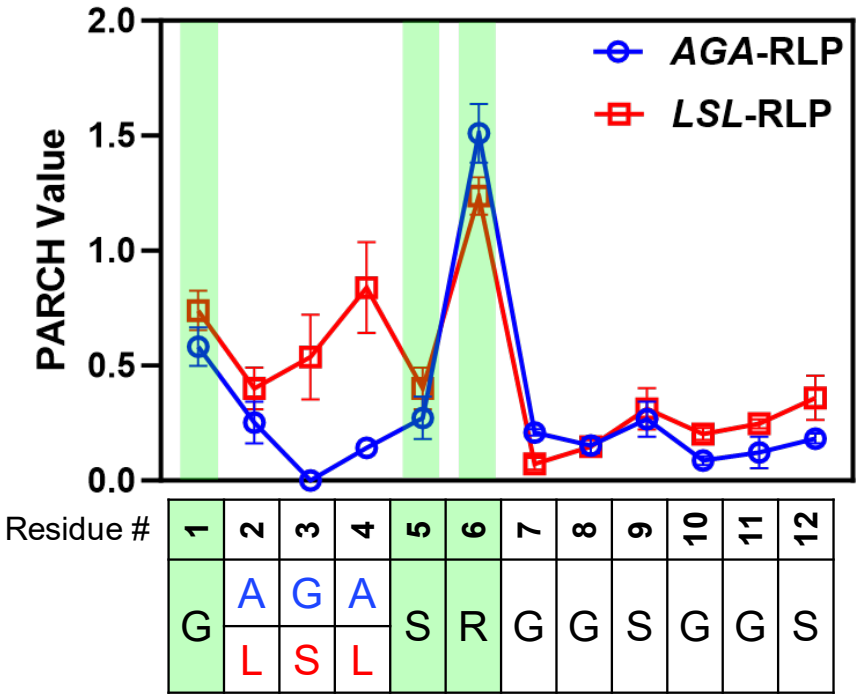

Figure S14. Computational analysis of the hydrophobicity of N-termini residues in unmodified RLPs using the PARCH scale method. In the absence of lipidation, *LSL*-RLP demonstrated lower hydrophobicity at residues A2-A4 (indicated by higher PARCH values) compared to AGA-RLP. However, the hydrophobicity of the flanking residues (G1, S5, R6) was comparable between both constructs before lipidation. We note that, unlike static hydropathy scales, PARCH values provide a quantitative assessment of each residue affinity for water due to chemical (e.g., amino acid identity and the effect of its neighboring residues) and topological features in the protein's three-dimensional geometry. In the absence of lipidation, the serine residue is likely increasing the hydrophilicity of nearby leucine residues.

References

1. M. Khodaverdi, M. S. Hossain, Z. Zhang, R. P. Martino, C. W. Nehls and D. Mozhdehi, *ChemSystemsChem*, 2021, **4**, e2100037.
2. A. De Marco, N. Berrow, M. Lebendiker, M. Garcia-Alai, S. H. Knauer, B. Lopez-Mendez, A. Matagne, A. Parret, K. Remans and S. Uebel, *Nat. Commun.*, 2021, **12**, 2795.
3. V. Zai-Rose, S. J. West, W. H. Kramer, G. R. Bishop, E. A. Lewis and J. J. Correia, *Biophys. J.*, 2018, **115**, 1431-1444.
4. B. Vrhovski, S. Jensen and A. S. Weiss, *Eur. J. Biochem.*, 1997, **250**, 92-98.
5. A. Peyret, E. Ibarboure, J.-F. Le Meins and S. Lecommandoux, *Adv. Sci.*, 2018, **5**, 1700453.
6. A. Roy, A. Kucukural and Y. Zhang, *Nat. Protoc.*, 2010, **5**, 725-738.
7. J. Yang, R. Yan, A. Roy, D. Xu, J. Poisson and Y. Zhang, *Nat. Methods*, 2015, **12**, 7-8.
8. J. Yang and Y. Zhang, *Nucleic Acids Res.*, 2015, **43**, W174-W181.
9. S. Jo, T. Kim, V. G. Iyer and W. Im, *J. Comput. Chem.*, 2008, **29**, 1859-1865.
10. J. Lee, X. Cheng, J. M. Swails, M. S. Yeom, P. K. Eastman, J. A. Lemkul, S. Wei, J. Buckner, J. C. Jeong, Y. Qi, S. Jo, V. S. Pande, D. A. Case, C. L. Brooks, A. D. MacKerell, J. B. Klauda and W. Im, *J. Chem. Theory Comput.*, 2016, **12**, 405-413.
11. J. Lee, M. Hitzenberger, M. Rieger, N. R. Kern, M. Zacharias and W. Im, *J. Chem. Phys.*, 2020, **153**, 035103.
12. J. Huang, S. Rauscher, G. Nawrocki, T. Ran, M. Feig, B. L. de Groot, H. Grubmuller and A. D. MacKerell, Jr., *Nat. Methods*, 2017, **14**, 71-73.
13. M. J. Abraham, T. Murtola, R. Schulz, S. Páll, J. C. Smith, B. Hess and E. Lindahl, *SoftwareX*, 2015, **1-2**, 19-25.
14. G. Bussi, D. Donadio and M. Parrinello, *J. Chem. Phys.*, 2007, **126**, 014101.
15. H. J. C. Berendsen, J. P. M. Postma, W. F. van Gunsteren, A. DiNola and J. R. Haak, *J. Chem. Phys.*, 1984, **81**, 3684-3690.
16. M. Parrinello and A. Rahman, *J. Appl. Phys.*, 1981, **52**, 7182-7190.
17. J. Ji, B. Carpentier, A. Chakraborty and S. Nangia, *J. Chem. Theory Comput.*, 2023, DOI: 10.1021/acs.jctc.3c00106.
18. V. The PyMOL Molecular Graphics System and L. Schrödinger, 2015.
19. W. Humphrey, A. Dalke and K. Schulten, *J. Mol. Graphics*, 1996, **14**, 33-38.
20. N. Michaud-Agrawal, E. J. Denning, T. B. Woolf and O. Beckstein, *J. Comput. Chem.*, 2011, **32**, 2319-2327.